

Thermoelectric interferometry on a Quantum Point Contact

B. Brun^{1*}, F. Martins^{1*}, S. Faniel¹, A. Cavanna⁴, C. Ulysse⁴, A. Ouerghi⁴, U. Gennser⁴,
D. Mailly⁴, P. Simon⁵, S. Huant², M. Sanquer³, H. Sellier², V. Bayot¹ & B. Hackens¹

¹*IMCN/NAPS, Université catholique de Louvain,
B-1348 Louvain-la-Neuve, Belgium*

²*Université Grenoble Alpes, CNRS,
Institut Néel, 38000 Grenoble, France*

³*Université Grenoble Alpes, CEA,
INAC-Phelips, 38000 Grenoble, France*

⁴*Centre de Nanosciences et Nanotechnologies (C2N) CNRS,
Route de Nozay, F-91460 Marcoussis, France*

⁵*Laboratoire de Physique des Solides, Bâtiment 510,
Université Paris Sud, F-91405 Orsay, France*

** Contributed equally to this work*

(Dated: June 21, 2022)

We introduce a new scanning probe technique derived from scanning gate microscopy (SGM) in order to investigate thermoelectric transport in two-dimensional semiconductor devices. The thermoelectric scanning gate microscopy (TSGM) consists in measuring the thermoelectric voltage induced by a temperature difference across a device, while scanning a polarized tip that locally changes the potential landscape. We apply this technique to investigate thermo-electric transport in a quantum point contact (QPC). We evidence large differences between SGM and TSGM signals in the low density regime of the QPC, where electron interactions are expected to be strong. We reveal from this set of measurements that Mott's law relating the thermopower to the conductance fails in this regime. In particular, a large phase jump appears in the interference fringes recorded by TSGM, which is not visible in SGM. We explain this difference of sensitivity using a microscopic model of the QPC, which includes the presence of a resonant level resulting from a spontaneous localization of electrons in the QPC channel at low transmission. This work demonstrates that combining scanning gate microscopy with thermoelectric measurements offers new information not available only with SGM, and thus provides deep understanding of the way the system transmission varies with energy, both in amplitude and in phase.

I. INTRODUCTION

In the context of emerging quantum technology and in view of the increasing care for energy harvesting, thermoelectric transport in nanomaterials and nanodevices has recently regained interest^{1,2}, leading to novel quantum thermal devices such as caloritronics interferometers³. The ability to accurately measure heat transport in two-dimensional systems⁴ and atomic junctions⁵ improved our global understanding of quantum thermodynamics, and shed light on mechanisms at play in complex many-body problems⁶⁻⁸. Investigating these thermal effects at the local scale is challenging, but lots of efforts are also made in this direction. As an example, heat dissipation was recently mapped inside a graphene nanodevice with unprecedented thermal and spatial resolutions⁹, unveiling new mechanisms responsible for current-to-heat conversion in graphene¹⁰.

Here we introduce a new scanning probe technique based on the Seebeck effect, in order to investigate the temperature-to-voltage conversion at the local scale within a quantum device^{11,12}. This probe, which we call Thermoelectric Scanning Gate Microscopy (TSGM), is applied to study the puzzling low-density regime of quantum point contacts (QPC)^{13,14}. Our experiments unveils unexpected features in the thermopower that cannot be addressed via conductance measurements. We explain

these deviations by the existence of an emergent resonant state with a very peculiar dependence on the QPC opening. This observation may help to understand better the nature of the conductance and thermoelectric anomalies in QPCs.

QPCs are quasi-one-dimensional ballistic channels in high-mobility two-dimensional electron gases (2DEG). Their conductance curves versus split-gate voltage show quantized plateaus at integer multiples of $2e^2/h$ as a consequence of ballistic transport¹⁵, but also show anomalous features which are believed to result from electron-electron (e-e) interactions. The conductance exhibits a shoulder-like feature known as the 0.7 anomaly¹⁶, which disappears as the temperature is lowered, and the differential conductance exhibits a zero-bias peak at very low temperature, known as the zero-bias anomaly (ZBA)¹⁷. Many different models have been proposed to explain these anomalies, but after decades of tremendous investigations, their exact microscopic origin still remains a matter of intense debate¹⁶⁻²³.

The thermoelectric properties of QPCs have also been studied²⁴ and were shown to be excellent probes of quantum confinement effects. The Seebeck coefficient $S = (\frac{\partial V}{\partial T})_{I=0}$, which relates the variations of voltage V to the temperature T in absence of current, has been shown to oscillate with the number of transmitted modes²⁵, and similarly for the thermal conductance and Peltier

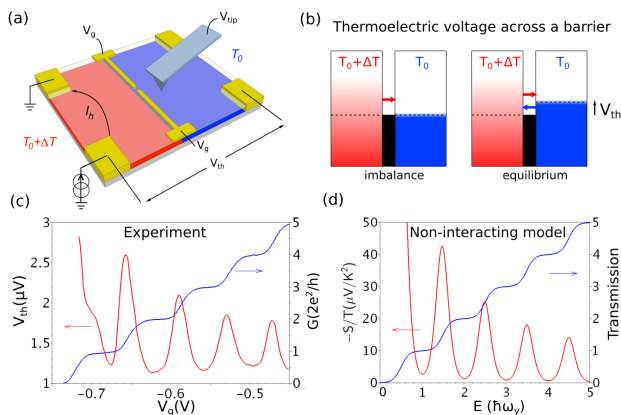


FIG. 1. (a) Scheme of the TSGM experiment: one side of the device is brought to higher temperature and the thermovoltage is recorded while scanning the polarized tip. (b) Seebeck effect across a barrier (black region): red and blue bars illustrate the energy distribution of charge carriers on the hot and cold sides. If transmission is energy-dependent, fluxes of hot and cold carriers are imbalanced. At equilibrium, a charge accumulation on the cold side restores a total balance of fluxes: this builds the thermovoltage V_{th} . (c) Differential conductance G , measured using a 4-probes technique at 25 mK (blue) and thermovoltage measured using a heating current of 180 nA (red) versus gate voltage V_g . (d) Theoretical transmission (blue) and Seebeck coefficient (red) calculated from the saddle-point model¹⁵ versus energy, for $\omega_x/\omega_y = 0.6$.

coefficients²⁶. In a single-electron picture, S is linked to the conductance G through Mott's relation²⁷:

$$S^M(\mu, T) = -\frac{\pi^2 k_B^2 T}{3e} \frac{1}{G(\mu, T)} \frac{\partial G(\mu, T)}{\partial \mu}, \quad (1)$$

where μ is the chemical potential. However, the thermopower is predicted to be sensitive to e-e interactions, and often reveals different information compared to the conductance. For example, in the case of Coulomb blockade, thermopower measurements probe the excitation spectrum rather than the addition spectrum^{28,29}. Since the thermopower is sensitive to the slope of the local density of states (DOS), it may be a useful probe of correlated behavior^{30,31}, which makes it very relevant in the case of QPC anomalies. Large deviations from Eq.(1) have indeed been reported in QPCs below the first conductance plateau³², and were presumably attributed to the important role of e-e interactions in this regime.

In this paper, we present an additional perspective on the low-transmission regime of QPCs, through interferometric Seebeck measurements performed with our novel TSGM technique. This new microscopy mode is a variant of the scanning gate microscopy (SGM) where the negatively polarized tip of a low-temperature scanning probe microscope is scanned above the surface, while recording tip-induced changes in the device's conductance^{33,34}. In TSGM, the device's Seebeck coefficient S is recorded instead of its electrical conductance³⁵. One of the two electron reservoirs is heated using a low frequency AC

current and the thermovoltage V_{th} across the device is measured as a function of the tip position (Fig.1a). The Seebeck coefficient is obtained as $S = V_{th}/\Delta T$ where ΔT is the temperature difference (Fig.1b).

In SGM images of QPCs, when the tip voltage is chosen such as to locally deplete the 2DEG, it generates fringes spaced by half of the Fermi wavelength due to Fabry-Pérot interference between the depleted region below the tip and the constriction defined by the split gate^{33,36,37}. By studying the behavior of these fringes in both G and S signals, we show that they reveal qualitatively different behaviors near the QPC pinch-off. These differences cannot be explained in the framework of Mott's relation (Eq.(1)), and we show that they arise from the different connection of G and S to the slope of the density of states at the Fermi energy. By developing a phenomenological 1D model we find that these differences can be understood as originating from the contribution of a localized state forming in low density regions of the QPC. As the QPC opens, the localized state is favored and its energy drops just below the Fermi level. For further QPC opening, the localized state stays pinned to the Fermi energy.

This demonstrates that TSGM has a great potential to precisely characterize the transmission function of mesoscopic systems, and brings information that elude standard transport measurements.

II. PRINCIPLE OF THERMOELECTRIC SCANNING GATE MICROSCOPY

The device chosen to illustrate this new experimental technique is a QPC, defined in a GaAs/AlGaAs heterostructure by a 270-nm-long and 300-nm-wide gap of a Ti/Au split gate. The 2DEG located 105 nm below the surface has $2.5 \times 10^{15} \text{ m}^{-2}$ electron density and $1.0 \times 10^6 \text{ cm}^2/(\text{V.s})$ electronic mobility at low temperature. The device is thermally anchored to the mixing chamber of a dilution fridge in front of a cryogenic scanning probe microscope³⁸ and cooled down to a base temperature of 25 mK. The four-probe differential conductance is measured by a lock-in technique using a 10 μV excitation. A series resistance of 200 Ω is subtracted from all data in order to have the first conductance plateau at $2e^2/h$. The lever-arm parameter of the split gate $\alpha = 54 \text{ meV/V}$ is deduced from the non-linear spectroscopy of the QPC subbands separated by $\Delta E = 3.5 \text{ meV}$ (see supplemental materials).

To measure the Seebeck coefficient of the QPC, we use the electron-heating technique depicted in Fig. 1a. We inject an AC current at 7.17 Hz between two contacts on the same side of the QPC, and record the voltage across the QPC using a lock-in detection at twice the heating frequency (14.34 Hz), in order to be sensitive to the dissipated power only and avoid any contribution related to the electrical conductance. The thermovoltage recorded versus gate voltage V_g is shown in Fig. 1c together with the measured conductance curve. As expected theoreti-

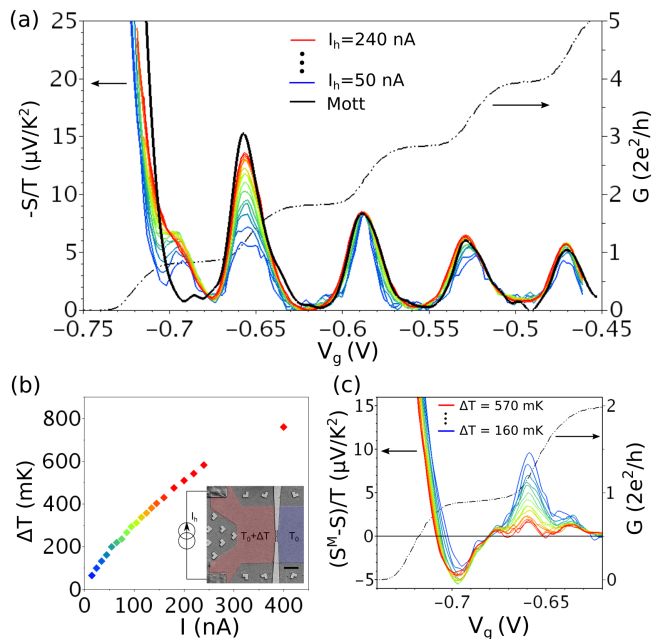


FIG. 2. (a) Black curve: $-S^M/T$ calculated using Mott’s law from the $G(V_g)$ curve at 25 mK (dashed line). Colored curves: $-S/T = (V_{th}/\Delta T)/T_{average}$ scaled to the black curve at the third peak summit using ΔT as the only fitting parameter. Heating currents range from 50 to 240 nA (blue to red). (b) Temperature difference ΔT as a function of the heating current. Inset: Electron microscope image of the device. The scale bar is $5 \mu\text{m}$. (c) $S/T - S^M/T$ for temperature differences from 160 to 570 mK (blue to red) as a function of V_g . Same data as in (a).

cally, the thermovoltage oscillates between minimum values when the QPC is on a plateau and maximum values for transitions between plateaus. For comparison, the transmission and Seebeck coefficients expected from a non-interacting saddle-point model¹⁵ are plotted in Fig. 1d.

A crucial issue in thermopower measurements is to relate the applied heating current to an actual temperature difference ΔT . To evaluate this quantity, we use two independent methods. First, we use Mott’s law for high densities, assuming that it is valid when more than 2 modes are transmitted through the QPC, and compare quantitatively the measured value S with that predicted by Mott’s law S^M . This comparison indicates the existence of a heating-current-dependent but gate-voltage-independent background in the measured signal (see supplemental materials).

With this background contribution removed, the measured Seebeck coefficient should be given by Mott’s relation applied to the measured conductance (black curve Fig. 2a). This is well verified for the third to fifth transitions, the only fitting parameter being the temperature difference. Fig. 2b shows the temperature differences deduced from these assumptions, ranging from 100 to 800 mK for heating currents from 15 to 400 nA. Second, we

compare these extracted values with estimates obtained from the temperature and current dependence of the Shubnikov-de-Haas oscillations in our sample, and find a good agreement (see supplemental materials). Note that the temperature difference is always larger than the average temperature, such that the system is far from the linear regime. Nevertheless, it has been shown that Mott’s law holds even in this highly non-linear regime, provided that ΔT is smaller than the subbands spacing and smearing³⁹.

Interestingly, the electronic temperature in the middle of the heated reservoir evolves sub-linearly with the heating current I_h , whereas one could naively expect a I_h^2 dependence related to the dissipated Joule power. This can be explained by the non-linear temperature dependence of heat losses in 2DEGs, mostly due to phonon emission⁴⁰ and electron out-diffusion in the ohmic contacts^{4,7}. These competing losses yield a non-uniform temperature profile and a sub-linear dependence on I_h of the local temperature far away from the ohmic contacts⁴¹.

In Fig. 2a, the correspondence between S and S^M does not hold when less than three QPC modes are transmitted, with two distinct features highlighted by the plot of their difference (see Fig. 2c): (i) In the transition from the first to second plateau ($V_g \sim -0.66 \text{ V}$), a large difference between S and S^M arises as ΔT is lowered below 500 mK; (ii) In the transition from pinch-off to the first plateau and on the first plateau itself ($V_g \sim -0.74 \text{ V}$ to -0.68 V), the discrepancies are observed for all the studied ΔT , and the difference $S - S^M$ changes sign in this range. Near the very pinch-off, the two values differ by a very large amount that increases with lowering ΔT . The local investigation using TSGM reported in this paper will focus on this specific regime.

Differences between S and S^M in the low-density regime of QPCs have already been reported in Ref.³². In that work, a local minimum was observed in the thermopower at the position of the 0.7 anomalous conductance plateau at 2 K, as expected from Eq.(1). However this minimum was shown to disappear into a shoulder at the lowest temperature of 300 mK, whereas the 0.7 plateau was still present (deviation from Eq.(1)). Here, with a base temperature of 25 mK, the conductance curve does not show any 0.7 plateau, an absence related to the emergence of a zero-bias anomaly that restores perfect transmission through the Kondo effect present in QPCs^{19,21}. Hence, the thermopower observations are different, though still in contradiction with Mott’s relation, with a minimum below the first plateau (blue curve in Fig. 2a around $V_g = -0.7 \text{ V}$) that disappears for ΔT around 500 mK.

III. RESULTS

We now report on the TSGM experiment, i.e. the investigation of thermoelectric transport in presence of the

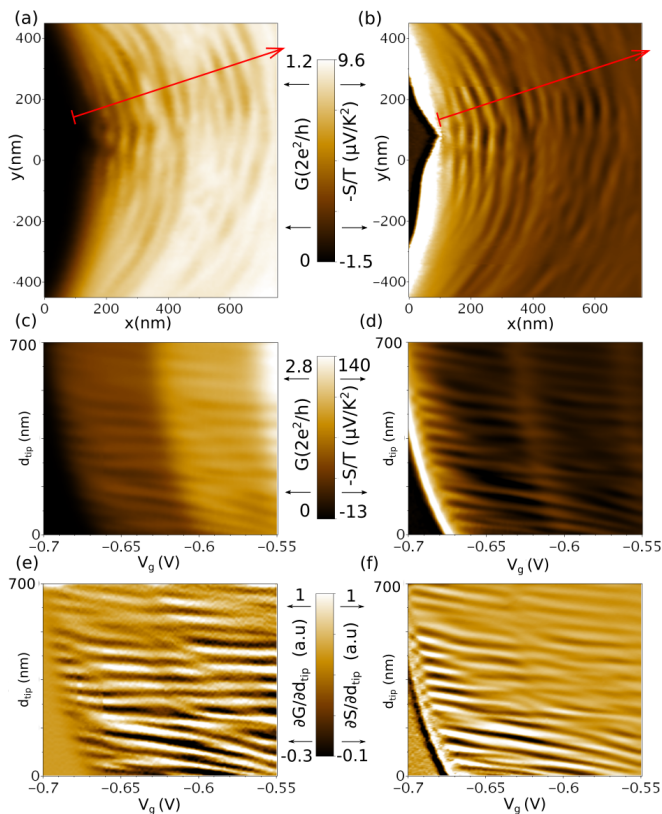


FIG. 3. (a) SGM image recorded when the QPC is open on the first plateau ($V_g = -0.66$ V): conductance G as a function of tip coordinates. The QPC center is located at $(-150 ; 0)$ nm on the left side of the image. (b) TSGM image of the thermopower in the same conditions, but recorded in a second pass while heating the reservoir on the opposite side of the scanning area. (c) Conductance and (d) thermovoltage as a function of gate voltage and tip position along the red line drawn in (a) and (b), recorded in the exact same conditions, but in separate tip scans. (e,f) Derivative of (a) and (b) with respect to tip position.

scanning gate. The tip is scanned 50 nm above the sample surface with an applied voltage of -6V, which locally depletes the 2DEG. Fig. 3 shows the SGM and TSGM images obtained by recording successively the conductance and the thermoelectric voltage in two different tip scans. The conductance signal is recorded using an AC excitation of $10 \mu\text{V}$, and the thermovoltage using a heating current of 150 nA, corresponding to a temperature difference of 450 mK. Both images look very similar, presenting interference fringes due to the Fabry-Pérot cavity formed by the QPC and the tip-depleted region. The TSGM image provides to our knowledge the first observation in real space of a thermally-driven electron interferometer.

Despite their apparent similarities, these images carry distinct information and cannot be deduced one from another. Indeed, even in the range where Mott's relation (1) is valid, deducing the TSGM image $S(x_{tip}, y_{tip})$ from the SGM $G(x_{tip}, y_{tip})$ would require a knowledge of

how the transmission evolves with the chemical potential ($\partial G/\partial\mu$). Most of the time, this quantity is not available in GaAs 2DEG, since it requires a backgate to vary the global electron density^{42,43}, which is a real challenge in high-mobility GaAs heterostructures.

In Fig.2a, the chemical potential of the QPC itself was identified as being proportional to V_g , which is a reasonable approximation when considering only the QPC transmission. In TSGM images, the distant influence of the tip does not allow such an identification, since the studied system now consists of the QPC coherently coupled to the tip-induced Fabry-Pérot cavity. As a consequence, the chemical potential of the system is not linearly linked to V_g , and TSGM images provide a different information than what is obtained from SGM.

To illustrate these differences, we study the evolution of the interference fringes as a function of the QPC opening. The conductance G and the thermovoltage V_{th} are recorded separately while scanning the tip along the line shown in Fig. 3(a,b), using an excitation of $15 \mu\text{V}$ and a temperature difference of 450 mK for G and S measurements, respectively. The evolution of the interference fringes with V_g is shown in Fig.3(c,d), for the conductance and thermovoltage signals. The fringes are similar in both signals but are superimposed on two very different background signals : a series of conductance plateaus for G , and a series of peaks for V_{th} (see Fig.2), including a very strong peak at the QPC pinch-off. To highlight the fringes' evolution with V_g , we derive both signals with respect to d_{tip} and plot the results in Fig.3(e,f). In these maps, we observe a complex evolution of the interference fringes, which looks globally similar in G and S , though few differences can be detected.

In the following, we focus on the very pinch-off, where S and S^M differ by a large amount (Fig. 2c). In this regime, the conductance oscillations follow a monotonic behavior (Fig.4c), i.e. their phase evolves monotonically with gate voltage, whereas the thermopower oscillations exhibit an abrupt phase shift at a conductance of about $0.25 \times 2e^2/h$ (Fig. 4d), which can already be surmised in Fig.3(d,f). A Fourier analysis (Fig. 4e) indicates that the phase shift observed in the thermopower is almost π . Similar phase shifts have been observed in the conductance signal in many different devices during our previous experiments⁴⁴. However they were observed at higher transmission, close to the first conductance plateau. Here the phase shift is observed in the thermopower at very low transmission, where no phase shift is present in the conductance.

IV. THERMOPOWER OF A LOCALIZED STATE : A SIMPLE MODEL

Phase shifts in the conductance have been attributed to the presence of spontaneously localized charges in the QPC channel^{22,45} (detailed discussion in supplemental materials). This interpretation arose from the analogy

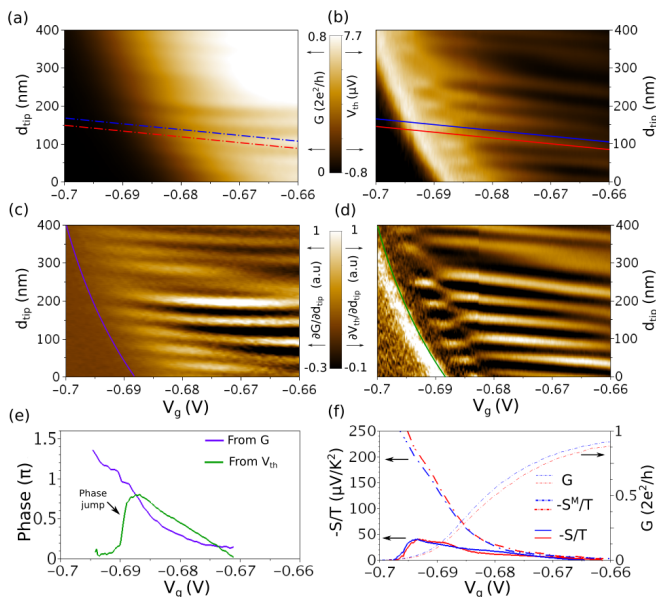


FIG. 4. (a) Conductance and (b) thermovoltage as a function of gate voltage and tip position along the red line drawn in Fig. 3, where d_{tip} here denotes tip position between 250 and 650 nm in Fig.3c-f. (c,d) Derivative of (a) and (b) with respect to tip position. (e) Phase of the interference fringes as a function of gate voltage extracted from the conductance (purple) and thermovoltage (green), following the pinch-off lines shown in (c) and (d) to account for cross-talk effect. (f) Line profiles of G , $-S^M/T$ and $-S/T$ extracted along the red and blue lines in (a) and (b).

with Aharonov-Bohm interferometers containing a quantum dot in one arm, where the interference pattern experiences a phase shift by π whenever one charge is added to the quantum dot⁴⁶, and by $\pi/2$ in the Kondo regime⁴⁷. Similarly, the phase shift observed here by TSGM at very-low transmission may also be attributed to the presence of localized charges in the constriction. Indeed, several evidences for the existence of bound states in QPCs near pinch-off have been reported^{48–52}, and predicted to spontaneously form as a consequence of e-e interaction by several numerical studies^{53–57}.

To explore how such localized states may affect the Seebeck coefficient we study an effective 1D model of transmission through the QPC. We model the gate-controlled potential in the QPC by a barrier with transmission rate Γ_L and we assume the presence of a spontaneously-localized state on the right side of the barrier, at an energy ϵ_0 , separated from the right reservoir by a barrier with transmission rate Γ_R (Fig.5a). This scenario has been proposed in Ref.⁵⁸ to explain the presence of QPC conductance anomalies down to very low conductance. This is also consistent for example with the results of local spin density functional theory presented in Ref.¹⁸, where two charges are shown to be localized on both sides of the main barrier at low density. Classical electrostatic simulations also confirm that at low QPC transmission, two one-dimensional regions form on both

sides of the channel, where the density is low enough to induce Wigner crystallization⁵⁹ (see supplemental materials). Though this would lead to two distinct charges, one on each side of the main barrier, we include only the right-side one in the model since the Fabry-Pérot cavity is sensitive only to the resonant level that is well coupled to it, the other being “hidden” by the main barrier²². We also model the tip as a distant scatterer of transmission amplitude $T_{tip} = 0.99$, whose distance from the resonant level D_{tip} can be varied. The expression of the energy-dependent transmission $T(E)$ through the whole system can then be calculated exactly as presented in Ref.²². We assume that the system is in the linear response regime, such that $\Delta T \ll T$ and $eV \ll E_F$. In this approximation, G and S respectively express in the Landauer framework as:

$$G = \frac{2e^2}{h} L_0 \quad (2)$$

$$S = -\frac{1}{|e|T} \frac{L_1}{L_0} \quad (3)$$

where

$$L_m = \int_{-\infty}^{+\infty} (E - \mu)^m \left(\frac{\partial f}{\partial E} \right) T(E) dE, \quad (4)$$

and $f(E)$ is the Fermi distribution.

We first show that the behaviors with respect to the tunneling rates of asymmetric barriers are very different for G and S (Fig.5b-c). For a fixed tunneling rate $\Gamma_R = 0.2$ (in units of the hopping term t), the effect of a decrease in Γ_L is opposite for G and S : it tends to decrease G , which is dominated by the lowest tunneling rate, but to increase S on both sides of the resonance since it is sensitive to the resonance sharpness, inversely proportional to $\Gamma_{tot} = \Gamma_L + \Gamma_R$.

In view of this effect, we find that a pinning/unpinning of a localized state at the Fermi level can reproduce the phase shift observations, suggesting the following scenario. We assume that the resonant state is very well coupled to the right lead ($\Gamma_R = 1$) and that it can evolve independently of Γ_L and Γ_R . As the QPC is progressively opened from the pinch-off (increasing of Γ_L), the energy of the resonant state ϵ_0 evolves as follows: (1) at $\Gamma_L = 0$, ϵ_0 lies well above μ , and no electron can localise in the 1D region. (2) As Γ_L increases, the energy cost of the electron localisation in the barrier is reduced, and ϵ_0 drops until it reaches the Fermi level. For our model parameters, this occurs at $\Gamma_L = 0.1$ (dashed line in Fig.5d). (3) Opening the QPC further does not change ϵ_0 , but the level stays pinned close to μ , up to the point where $\Gamma_L = \Gamma_R$ and the transmission reaches unity. The physical reason for the pinning is discussed in section V and supplemental materials. In this scenario, the conductance behaves as normally expected for a QPC (Fig.5d): the resonance is almost invisible as it appears close to the pinch-off. It also gives no discernible signature in the interference fringes, since it occurs at very low transmission (Fig.5f and 5h). The high sensitivity of S results

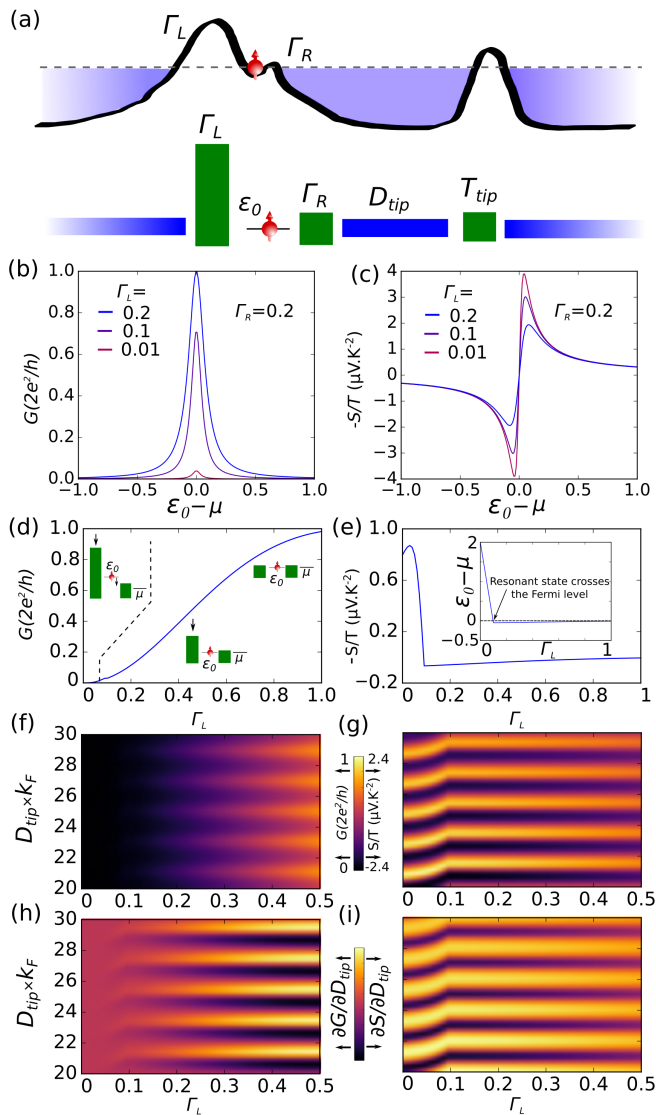


FIG. 5. (a) Up: typical energetic potential which could lead to the proposed scenario: spontaneously localized states form on both sides of the main QPC barrier. Down: Scheme of the 1D model including, from left to right, the QPC barrier (Γ_L), the localized state (ϵ_0 and Γ_R), and the tip-induced cavity (D_{tip} and T_{tip}). (b) Conductance of its energy relative to μ for fixed $\Gamma_R = 0.2$ and $\Gamma_L = 0.2$ (blue) to 0.01 (red). (c) Seebeck coefficient in the same configuration. (d) Conductance evolution with Γ_L assuming that the resonant level, perfectly coupled to the right lead ($\Gamma_R = 1$), crosses μ at $\Gamma_L = 0.1$ and then stays just below the Fermi level while the QPC opens. (e) Seebeck coefficient in the exact same scenario. (f,g): Evolution of the Fabry-Pérot interference in this scenario: conductance (f) and Seebeck coefficient (g) as a function of tip distance and Γ_L . (h,i): Derivative of G and S with respect to D_{tip} .

from the strong variation of the transmission with energy when the resonance approaches the Fermi level.

The phase shift induced by the drop of ϵ_0 below μ is highly visible in S , and is due to the Breit-Wigner

like resonance of the localized state, that induces a total π phase shift when the level crosses the Fermi energy. Since the Fabry-Pérot cavity probes twice the resonant level phase shift in case of a strong coupling on the cavity side²², the total phase shift should be 2π . However assuming a fall of ϵ_0 just below μ but staying at this value, the phase shift remains half the value of 2π and may correspond to the experimentally observed π value.

V. DISCUSSION

One may wonder whether the resonant level introduced in the model is really located in the QPC, or if it could instead be located away from the QPC, as a result of potential fluctuations induced by remote ionized dopants. Such a resonant state, away from the QPC, but still in the cavity, would also produce a phase shift of the interference pattern. However in that scenario, the resonant level ϵ_0 would not be affected by the QPC gate voltage, and there is no reason for it to evolve with Γ_L , neither to stay pinned to μ after a given opening. Experimentally, the π phase shift evolves with gate voltage following exactly the pinch-off line (Fig.4d), which means that this resonant state must be directly in the QPC channel. The fact that this resonant state stays pinned to the Fermi energy for further QPC opening suggests that its emergence is not related to disorder, but it may instead spontaneously appear because of the strong Coulomb repulsion at low density, as predicted numerically for quasi unidimensional quantum wires^{53-55,57}. In particular, this hypothesis can be supported by the numerical study performed in Ref.⁵⁷, where the authors showed that a few electrons can localize at low electron density in a QPC, and separate from the leads by a tunnel barrier that reduces as the density is increased. This picture is in line with the phenomenological behavior of the resonant level proposed here to explain our observation, pointing towards a spontaneous localization of electrons rather than a disorder-induced resonant level.

VI. CONCLUSION

In conclusion, we introduced a new scanning probe technique to image thermoelectric transport through a QPC. By scanning the polarized tip in front of the QPC, we imaged for the first time interference of electrons driven by a temperature difference, in analogy with the well-established SGM experiments where the electron flow is driven by a voltage difference. In addition, we showed that in the very-low-conductance regime, the thermopower interference fringes experience an abrupt phase shift, invisible in the conductance signal. We propose a simple 1D model to show that this phase shift and its characteristics can be explained by the existence of a localized state forming in the QPC channel at low density, and that stays pinned to the

Fermi energy of the leads as the first QPC mode opens. The fact that this localized state signature is hidden in conductance measurements but highly visible in the Seebeck coefficient is explained by its sharpness and occurrence at low transmission. The peculiar evolution of this resonant level with the QPC opening suggests that it results from a spontaneous localization rather than from disorder. This work illustrates that the combination of scanning gate microscopy and thermoelectric measurements can unveil elusive phenomena that escape transport measurements, and allows deep

investigation of the exact transmission evolution with energy. Importantly, this transmission coefficient is better characterized by TSGM not only in amplitude but also in phase, thanks to the interferometric measurement.

We thank J.-L. Pichard and A. Abbout for the original idea of the experiment. This work was supported by the “Crédit de Recherche” (CDR) grant no. J.0009.16 from the FRS-FNRS, and the French Agence Nationale de la Recherche (“ITEM-exp” project). B.B, F.M. and B.H. acknowledge support from the Belgian FRS-FNRS, S.F. received support from the FSR at UCL.

-
- ¹ M. Dresselhaus, G. Chen, M. Tang, R. Yang, H. Lee, D. Wang, Z. Ren, J.-P. Fleurial, and P. Gogna, *Adv. Mat.* **19**, 1043 (2007).
- ² J.-H. Jiang and Y. Imry, *Comptes Rendus Physique* **17**, 1047 (2016).
- ³ F. Giazotto and M. J. Martínez-Pérez, *Nature* **492**, 401 (2012).
- ⁴ S. Jezouin, F. D. Parmentier, A. Anthore, U. Gennser, A. Cavanna, Y. Jin, and F. Pierre, *Science* **342**, 601 (2013).
- ⁵ L. Cui, W. Jeong, S. Hur, M. Matt, J. C. Klöckner, F. Pauly, P. Nielaba, J. C. Cuevas, E. Meyhofer, and P. Reddy, *Science* **355**, 1192 (2017).
- ⁶ M. Banerjee, M. Heiblum, A. Rosenblatt, Y. Oreg, D. E. Feldman, A. Stern, and V. Umansky, *Nature* **545**, 75 (2017).
- ⁷ E. Sivre, A. Anthore, F. D. Parmentier, A. Cavanna, U. Gennser, A. Ouerghi, Y. Jin, and F. Pierre, *Nat. Phys.* **14**, 145 (2017).
- ⁸ B. Dutta, J. T. Peltonen, D. S. Antonenko, M. Meschke, M. A. Skvortsov, B. Kubala, J. König, C. B. Winkelmann, H. Courtois, and J. P. Pekola, *Phys. Rev. Lett.* **119**, 077701 (2017).
- ⁹ D. Halbertal, J. Cuppens, M. B. Shalom, L. Embon, N. Shadmi, Y. Anahory, H. R. Naren, J. Sarkar, A. Uri, Y. Ronen, Y. Myasoedov, L. S. Levitov, E. Joselevich, A. K. Geim, and E. Zeldov, *Nature* **539**, 407 (2016).
- ¹⁰ D. Halbertal, M. Ben Shalom, A. Uri, K. Bagani, A. Y. Meltzer, I. Marcus, Y. Myasoedov, J. Birkbeck, L. S. Levitov, A. K. Geim, and E. Zeldov, *Science* **358**, 1303 (2017).
- ¹¹ W. Thomson, *Proc. Roy. Soc. Edinburgh*, 91 (1851).
- ¹² D. K. C. M. Donald, *Thermoelectricity: An Introduction to the Principles* (John Wiley and Sons, Inc., New York, 1962).
- ¹³ B. J. van Wees, H. van Houten, C. W. J. Beenakker, J. G. Williamson, L. P. Kouwenhoven, D. van der Marel, and C. T. Foxon, *Phys. Rev. Lett.* **60**, 848 (1988).
- ¹⁴ D. A. Wharam, T. J. Thornton, R. Newbury, M. Pepper, H. Ahmed, J. E. F. Frost, D. G. Hasko, D. C. Peacock, D. A. Ritchie, and G. A. C. Jones, *Journal of Physics C: Solid State Physics* **21**, L209 (1988).
- ¹⁵ M. Büttiker, *Phys. Rev. B* **41**, 7906 (1990).
- ¹⁶ K. J. Thomas, J. T. Nicholls, M. Y. Simmons, M. Pepper, D. R. Mace, and D. A. Ritchie, *Phys. Rev. Lett.* **77**, 135 (1996).
- ¹⁷ S. M. Cronenwett, H. J. Lynch, D. Goldhaber-Gordon, L. P. Kouwenhoven, C. M. Marcus, K. Hirose, N. S. Wingreen, and V. Umansky, *Phys. Rev. Lett.* **88**, 226805 (2002).
- ¹⁸ T. Rejec and Y. Meir, *Nature* **442**, 900 (2006).
- ¹⁹ M. J. Iqbal, R. Levy, E. J. Koop, J. B. Dekker, J. P. de Jong, J. H. M. van der Velde, D. Reuter, A. D. Wieck, R. Aguado, Y. Meir, and C. H. van der Wal, *Nature* **501**, 79 (2013).
- ²⁰ F. Bauer, J. Heyder, E. Schubert, D. Borowsky, D. Taubert, B. Bruognolo, D. Schuh, W. Wegscheider, J. von Delft, and S. Ludwig, *Nature* **501**, 73 (2013).
- ²¹ B. Brun, F. Martins, S. Faniel, B. Hackens, G. Bachelier, A. Cavanna, C. Ulysse, A. Ouerghi, U. Gennser, D. Mailly, S. Huant, V. Bayot, M. Sanquer, and H. Sellier, *Nat. Commun.* **5**, 4290 (2014).
- ²² B. Brun, F. Martins, S. Faniel, B. Hackens, A. Cavanna, C. Ulysse, A. Ouerghi, U. Gennser, D. Mailly, P. Simon, S. Huant, V. Bayot, M. Sanquer, and H. Sellier, *Phys. Rev. Lett.* **116**, 136801 (2016).
- ²³ A. P. Micolich, *Journal of Physics: Cond. Matt.* **23**, 443201 (2011).
- ²⁴ P. Streda, *Journal of Physics: Cond. Matt.* **1**, 1025 (1989).
- ²⁵ L. W. Molenkamp, H. van Houten, C. W. J. Beenakker, R. Eppenga, and C. T. Foxon, *Phys. Rev. Lett.* **65**, 1052 (1990).
- ²⁶ L. W. Molenkamp, T. Gravier, H. van Houten, O. J. A. Buijk, M. A. A. Mabesoone, and C. T. Foxon, *Phys. Rev. Lett.* **68**, 3765 (1992).
- ²⁷ H. Mott, N.F. Jones, *The Theory Of The Properties Of Metals And Alloys* (Oxford University Press, 1936).
- ²⁸ C. W. J. Beenakker and A. A. M. Staring, *Phys. Rev. B* **46**, 9667 (1992).
- ²⁹ A. S. Dzurak, C. G. Smith, C. H. W. Barnes, M. Pepper, L. Martín-Moreno, C. T. Liang, D. A. Ritchie, and G. A. C. Jones, *Phys. Rev. B* **55**, R10197 (1997).
- ³⁰ D. Sanchez and R. Lopez, *Comptes Rendus de Physique* **17**, 1060 (2016).
- ³¹ D. Boese and R. Fazio, *Europhys. Lett.* **56**, 576 (2001).
- ³² N. J. Appleyard, J. T. Nicholls, M. Pepper, W. R. Tribe, M. Y. Simmons, and D. A. Ritchie, *Phys. Rev. B* **62**, R16275 (2000).
- ³³ M. A. Topinka, B. J. LeRoy, R. M. Westervelt, S. E. J. Shaw, R. Fleischmann, E. J. Heller, K. D. Maranowski, and A. C. Gossard, *Nature* **410**, 183 (2001).
- ³⁴ H. Sellier, B. Hackens, M. G. Pala, F. Martins, S. Baltazar, X. Wallart, L. Desplanque, V. Bayot, and S. Huant, *Semi-*

- conductor Science and Technology **26**, 064008 (2011).
- ³⁵ A. About, *Thermoelectric transport in quantum point contacts and chaotic cavities : thermal effects and fluctuations*, Ph.D. thesis, Université Paris VI (2011).
- ³⁶ M. P. Jura, M. A. Topinka, M. Grobis, L. N. Pfeiffer, K. W. West, and D. Goldhaber-Gordon, Phys. Rev. B **80**, 041303 (2009).
- ³⁷ A. A. Kozikov, C. Rössler, T. Ihn, K. Ensslin, C. Reichl, and W. Wegscheider, New Journal of Physics **15**, 013056 (2013).
- ³⁸ B. Hackens, F. Martins, S. Faniel, C. A. Dutu, H. Sellier, S. Huant, M. Pala, L. Desplanque, X. Wallart, and V. Bayot, Nat. Commun. **1**, 39 (2010).
- ³⁹ A. M. Lunde and K. Flensberg, Journal of Physics: Condensed Matter **17**, 3879 (2005).
- ⁴⁰ P. J. Price, Journal of Applied Physics **53**, 6863 (1982).
- ⁴¹ A. Mittal, R. Wheeler, M. Keller, D. Prober, and R. Sacks, Surface Science **361**, 537 (1996).
- ⁴² B. A. Braem, C. Gold, S. Hennel, M. Rslı, M. Berl, W. Dietsche, W. Wegscheider, K. Ensslin, and T. Ihn, New Journal of Physics **20**, 073015 (2018).
- ⁴³ B. A. Braem, F. M. Pellegrino, A. Principi, M. Rössli, S. Hennel, J. V. Koski, M. Berl, W. Dietsche, W. Wegscheider, M. Polini, T. Ihn, and K. Ensslin, ArXiv e-prints (2018), arXiv:1807.03177 [cond-mat.mes-hall].
- ⁴⁴ B. Brun, *Electron interactions in mesoscopic physics : Scanning Gate Microscopy and interferometry at a quantum point contact*, Ph.D. thesis, Université de Grenoble (2014).
- ⁴⁵ A. Freyn, I. Kleftogiannis, and J.-L. Pichard, Phys. Rev. Lett. **100**, 226802 (2008).
- ⁴⁶ A. Yacoby, M. Heiblum, D. Mahalu, and H. Shtrikman, Phys. Rev. Lett. **74**, 4047 (1995).
- ⁴⁷ M. Zaffalon, A. Bid, M. Heiblum, D. Mahalu, and V. Umansky, Phys. Rev. Lett. **100**, 226601 (2008).
- ⁴⁸ V. I. Puller, L. G. Mourokh, A. Shailos, and J. P. Bird, Phys. Rev. Lett. **92**, 096802 (2004).
- ⁴⁹ H. Steinberg, O. M. Auslaender, A. Yacoby, J. Qian, G. A. Fiete, Y. Tserkovnyak, B. I. Halperin, K. W. Baldwin, L. N. Pfeiffer, and K. W. West, Phys. Rev. B **73**, 113307 (2006).
- ⁵⁰ Y. Yoon, L. Mourokh, T. Morimoto, N. Aoki, Y. Ochiai, J. L. Reno, and J. P. Bird, Phys. Rev. Lett. **99**, 136805 (2007).
- ⁵¹ P. M. Wu, P. Li, H. Zhang, and A. M. Chang, Phys. Rev. B **85**, 085305 (2012).
- ⁵² S.-C. Ho, H.-J. Chang, C.-H. Chang, S.-T. Lo, G. Creeth, S. Kumar, I. Farrer, D. Ritchie, J. Griffiths, G. Jones, M. Pepper, and T.-M. Chen, Phys. Rev. Lett. **121**, 106801 (2018).
- ⁵³ O. P. Sushkov, Phys. Rev. B **64**, 155319 (2001).
- ⁵⁴ O. P. Sushkov, Phys. Rev. B **67**, 195318 (2003).
- ⁵⁵ L. Shulenburger, M. Casula, G. Senatore, and R. M. Martin, Phys. Rev. B **78**, 165303 (2008).
- ⁵⁶ S. A. Söfing, M. Bortz, I. Schneider, A. Struck, M. Fleischhauer, and S. Eggert, Phys. Rev. B **79**, 195114 (2009).
- ⁵⁷ A. D. Güçlü, C. J. Umrigar, H. Jiang, and H. U. Baranger, Phys. Rev. B **80**, 201302 (2009).
- ⁵⁸ Y. Ren, W. W. Yu, S. M. Frolov, J. A. Folk, and W. Wegscheider, Phys. Rev. B **82**, 045313 (2010).
- ⁵⁹ E. Wigner, Phys. Rev. **46**, 1002 (1934).

Thermoelectric interferometry on a Quantum Point Contact
- Supplemental materials -

B. Brun¹, F. Martins¹, S. Faniel¹, A. Cavanna⁴, C. Ulysse⁴, A. Ouerghi⁴, U. Gennser⁴, D. Maily⁴, P. Simon⁵, S. Huant², M. Sanquer³, H. Sellier², V. Bayot¹ & B. Hackens¹

¹*IMCN/NAPS, Université catholique de Louvain,
B-1348 Louvain-la-Neuve, Belgium*

²*Université Grenoble Alpes,
CNRS, Institut Néel,
38000 Grenoble, France*

³*Université Grenoble Alpes,
CEA, INAC-Pheliqs,
38000 Grenoble, France*

⁴*Centre de Nanosciences et Nanotechnologies (C2N) CNRS,
Route de Nozay,
F-91460 Marcoussis, France*

⁵*Laboratoire de Physique des Solides,
Bâtiment 510, Université Paris Sud,
F-91405 Orsay, France*

I. SUBBANDS ENERGY SPACING

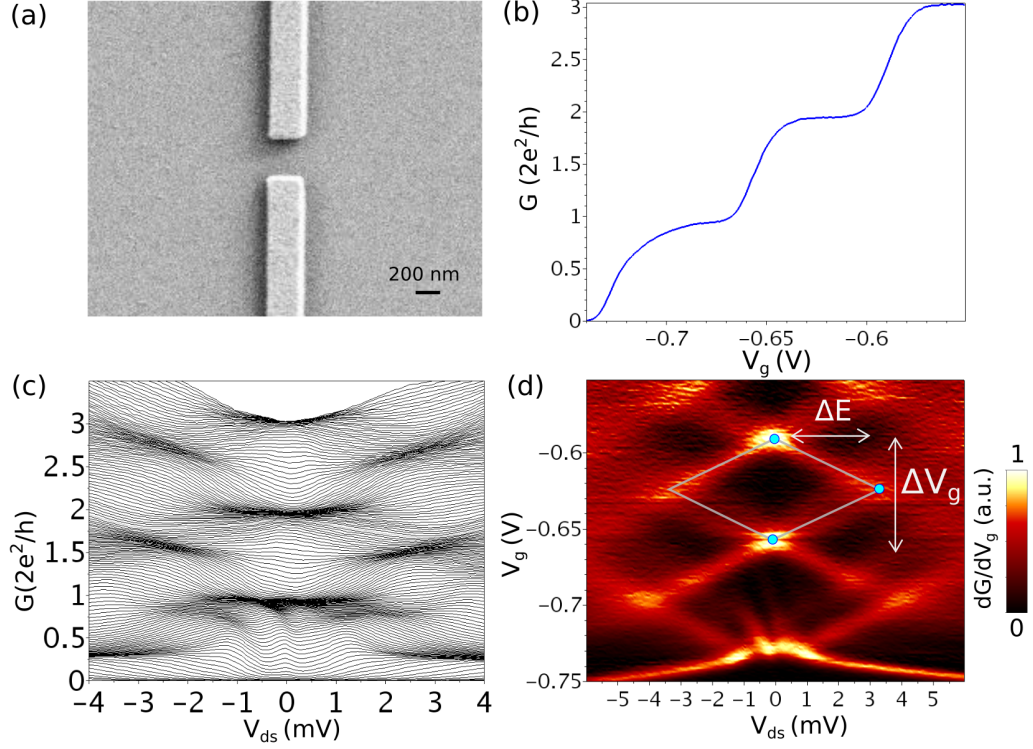


FIG. 1: **Lever-arm parameter of the split gate:** (a) Electron microscope image of the split gate defining the QPC in the 2DEG. (b) Differential conductance G versus gate voltage V_g , measured in 4-probes at 25 mK. (c) Non-linear conductance traces $G(V_{ds})$ for gate voltages spaced by 1.25 mV. (d) Derivative of G versus V_g as a function of V_{ds} and V_g , showing the energy spacing ΔE between the quasi-1D subbands, which are separated by ΔV_g in gate voltage.

The lever-arm parameter α of the split gate, relating the potential energy in the constriction to the voltage applied on the split gate, is deduced from the non-linear conductance traces shown in Fig. 1 (c) and (d). The energy spacing between the first and second subband is $\Delta E_{1-2} = 3.5$ meV, and corresponds to a change in gate voltage $\Delta V_g = 0.065$ V. The lever-arm parameter of the split gate is therefore taken as 54 ± 5 meV/V.

II. ZERO-BIAS CONDUCTANCE ANOMALY

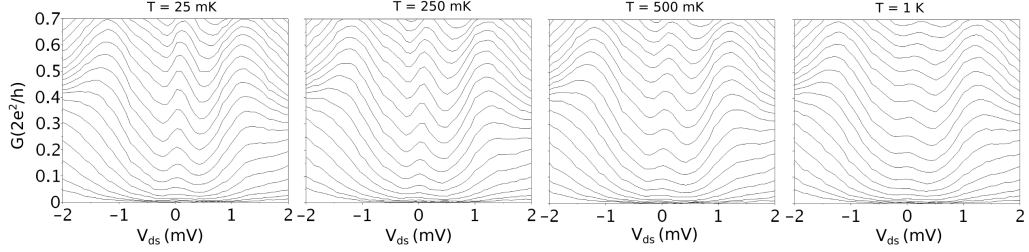


FIG. 2: **Evolution of the zero-bias anomaly with temperature:** Non-linear conductance traces $G(V_{ds})$ for gate voltages spaced by 1.25 mV versus DC source-drain bias V_{ds} , at 25 mK, 250 mK, 500 mK and 1 K.

The zero-bias anomaly is visible below the first conductance plateau. At a base temperature of 25 mK its full-width at half maximum is $\Delta V \sim 300 \mu\text{eV}$. This corresponds to a Kondo temperature $T_K = \frac{e\Delta V}{k_B} \sim 1.7$ K. The ZBA shades off for temperatures above 500 mK and has almost disappeared at 1 K.

III. BACKGROUND IN THE THERMOELECTRIC SIGNAL

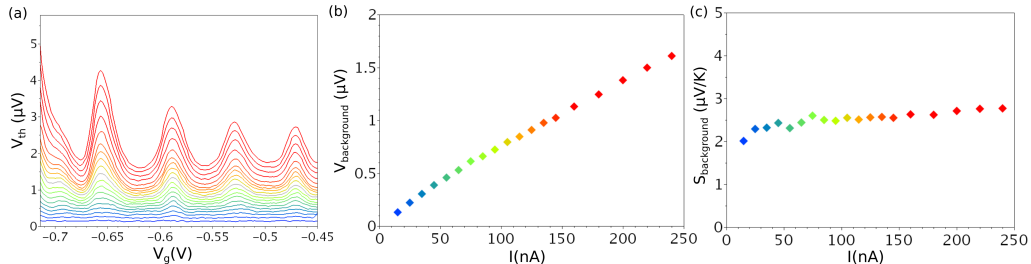


FIG. 3: **Temperature-dependent background in the thermoelectric voltage:** (a) Raw data of the measured V_{th} versus V_g , for heating currents ranging from 15 nA (blue curve) to 240 nA (red curve). (b) Minimum thermovoltage between the first and second thermovoltage peaks at $V_g = -0.62$ V, plotted as a function of the heating current. This value corresponds to the gate-voltage-independent background which is subtracted in Fig. 2a of the main paper before the evaluation of the temperature difference. (c) Seebeck coefficient of the background signal obtained by dividing the thermovoltage by the estimated temperature difference ΔT , extracted using the Mott's law (Fig. 2b of the main paper)

In our experimental setup, the thermoelectric voltage is measured between two ohmic contacts and includes several contributions : (i) the thermovoltage across the QPC which is the interesting signal, (ii) a thermovoltage in the 2DEG due to a temperature gradient inside the heated reservoir, and (iii) a thermovoltage at the junction between the heated 2DEG reservoir and the ohmic contact. We assume here that the ohmic contacts are thermalized at the fridge temperature. The thermovoltage at the QPC is the gate-voltage-dependent signal, whereas the two others contributions form the gate-voltage-independent signal, called background (see Fig. 3a). For each heating current, the background is defined as the thermovoltage value in the second minimum of the curve, at $V_g = -0.62$ V. Since the temperature of both reservoirs is always kept lower than the subband energy spacing ($\Delta E/k_B \sim 40$ K), we indeed have $dG/dV_g = 0$ on the plateaus, and the thermovoltage at the QPC should drop to zero. The dependence of this background on the heating current is shown in Fig. 3b. Using the evaluated temperature differences as a function of the heating current (see main paper), we can estimate the thermopower corresponding to the observed background

(Fig.3c), and we find a value around $2.5 \mu\text{V}/\text{K}$ which depends weakly on the heating current.

In the following, we discuss quantitatively the origin of this background signal. The thermopower of the 2DEG can be separated in two main contributions: the thermopower due to the phonons, usually called the phonon drag, and the diffusion thermopower, that can be expressed as:

$$S^d = \frac{\pi^2 k_B^2 T}{3eE_F} (p + 1) \quad (1)$$

where p represents the dependence of the electrons scattering rate with energy, that depends on the scattering mechanism but is close to unity¹. In our case, this expression yields $S^d = 0.1 \mu\text{V}/\text{K}$ at the lowest temperature, and rises up to $S^d = 0.5 \mu\text{V}/\text{K}$ for the largest applied temperature differences. The 2DEG diffusion thermopower can therefore not account alone for this background. The contribution of phonons could be invoked, but it is likely that the phonon drag does not contribute to the thermopower in our case, due to the sub-Kelvin temperature, regarding other works¹⁻³. The thermopower due to the ohmic contacts is not well characterized, and might be responsible for this background signal, together with a small contribution from the 2DEG as discussed above.

IV. TEMPERATURE ESTIMATED FROM SDH OSCILLATIONS

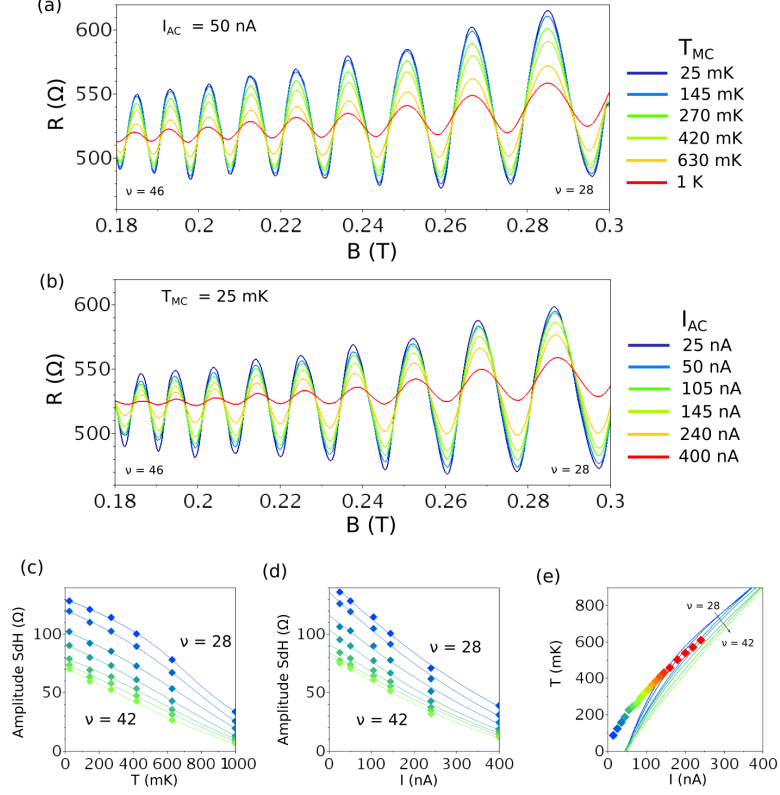


FIG. 4: **Temperature and AC current dependence of Shubnikov-de-Haas oscillations:** (a) Shubnikov-de-Haas oscillations for temperatures ranging from 25 mK to 1 K. The applied AC current is 50 nA and a series resistance of 2.4 k Ω is subtracted to account for filters and contacts resistance (2-probes measurements). (b) Shubnikov-de-Haas oscillations for AC current ranging from 25 nA to 400 nA at the base temperature of 25 mK. (c) Amplitude of SdH oscillations as a function of mixing chamber temperature, and polynomial fit for each Landau level. (d) Amplitude of SdH oscillations as a function of applied AC current, and polynomial fit for each Landau level. (e) Combination of the two polynomial fits to obtain temperature as a function of AC current. The temperature of the hot reservoir extracted from the thermovoltage analysis using the Mott's law is plotted as squares for comparison.

To reproduce the same geometry as in the thermopower measurement, the SdH oscillations (Fig. 4a and 4b) are measured between the two contacts located on the same side of

the QPC, and a split gate voltage lower than the depletion threshold is applied. We used $V_g = -0.65$ V corresponding to one mode open in the QPC but we checked that the results do not change if the QPC is closed at $V_g = -0.75$ V. Fig. 4e presents the estimation of the current-induced 2DEG temperature obtained from the analysis of the SdH oscillations amplitude versus temperature (Fig. 4c) and versus current (Fig. 4d). The estimated temperatures vary a bit with the filling factor, but remain in the same range. This estimation indicates a similar order of magnitude as the temperatures evaluated from the thermovoltage analysis using the Mott's law (squares). The similarities between the two methods disappear below 300 mK. This is not surprising as the temperature evolution of the SdH oscillations was measured with a large current of 50 nA to have a reliable signal, corresponding to a current-induced temperature of about 200 mK.

It shall also be noted that the temperature profile is expected to be non-uniform in the heated region⁴. Hence SdH oscillations may be affected by the overall temperature profile whereas the estimated temperature difference obtained from the QPC thermovoltage is sensitive to the local temperature in its close vicinity. This could account for the observed differences between the two methods.

The sub-linear dependence of the temperature difference on heating current (Fig. 4e here and Fig. 2b of the main paper) can be explained in the framework of heat dissipation in 2DEGs. When electrons are brought to an electronic temperature T_e higher than the phonon temperature T_{ph} they can lose energy via different mechanisms. The dominant ones at low temperatures are the phonon emission⁵, which evolves as T_e^5 , and the electron out-diffusion in the ohmic contacts, which evolves as T_e^2 as accurately verified down to the quantum limit of a single electronic channel^{6,7}. These competing losses yield a non-uniform temperature profile and a sub-linear dependence of the local temperature on the heating current⁴.

V. CORRELATION BETWEEN PHASE SHIFT AND CHANGE IN THE NUMBER OF LOCALIZED CHARGES

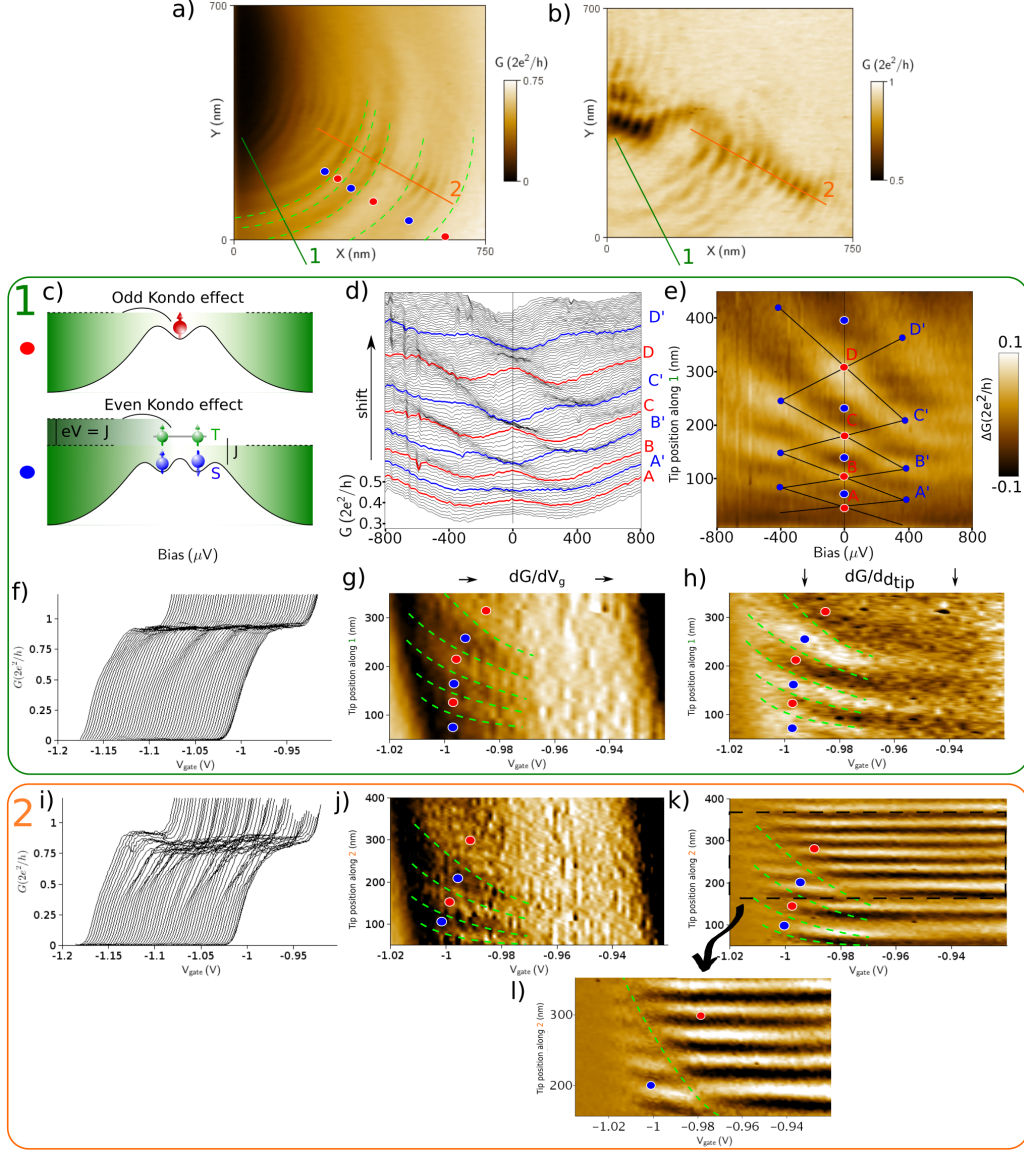


FIG. 5: **Correspondence between phase shifts in the interference fringes and changes in the number of localized charges, in a similar sample (see Ref.⁸):** (a,b) SGM maps of the conductance G for gate voltages: (a) below the first plateau at $V_g = -1$ V and (b) on the first plateau at $V_g = -0.95$ V. (c) Scheme of spontaneously localized charges with a net spin $S=1/2$ ground state (upper panel) and a net spin $S=0$ ground state (lower panel). (d) Differential conductance G versus source-drain bias at a fixed gate voltage $V_g = -1$ V for different tip positions from 0 to 450 nm along the line 1 indicated in (a,b). Successive curves are shifted upwards by $0.0075 \times 2e^2/h$. (e) Color plot of the same data as in (d) after subtraction of a smooth background to suppress the main gating effect of the tip. Peak positions are indicated by dots. The successive ZBA splittings give a checkerboard pattern. (f,i) Traces $G(V_g)$ for several tip positions along the lines 1 and 2 indicated in (a,b). The curves are shifted in V_g for clarity. (g,j) Color-plot of the same data, differentiated with respect to gate voltage ($\partial G/\partial V_g$). (h,k) Color-plot of the same data, differentiated with respect to tip position along these lines ($\partial G/\partial d_{tip}$). The different parities of the number of charges localized in the QPC are indicated by blue (even) and red (odd) dots. Green dashed lines represent changes by one electron charge. (l) Zoom of (k) showing a region with a single change in the charge number, highlighting a phase shift of the interference.

In Fig.5 we explain how the phase shifts of the interference fringes are connected with a change by one in the number of charges localized in the QPC. The QPC presented here has the same geometry as the one in the present paper but is a different sample. Its transport characteristic are detailed in ref.⁸. We describe here our understanding of this phenomenon, which is a generic feature and is not sample specific, and has also been reproduced since by an other group. (Beat Braem, ETH Zürich, *private communication*).

Below the first conductance plateau, the 1D electronic density in the QPC is so low that a definite number of charges spontaneously localize due to Coulomb repulsion, in a mechanism similar to Wigner crystallization. This number of charges can be changed by moving the tip in front of the QPC, which affects the QPC potential and the size of the crystal. This effect is visible as concentric rings in the SGM image recorded below the first plateau Fig.5a. These rings correspond to alternating single-peak or split-peak zero-bias anomalies (Fig.5d) matching respectively with an odd or even number of localized charges. Dashed lines on Fig.5a indicate tip positions leading to a change in the number of localized charges.

The number of localized charges can also change as a function of QPC opening (with V_g ,

not shown here). The modulations visible in the conductance traces at zero bias are really generic and correspond to a ZBA that spontaneously splits as the QPC opens or its shape is varied⁹⁻¹¹. The tip position and gate voltage affect differently the number of localized charges but *loci* of changes in this number can be followed in colormaps of conductance versus V_g and d_{tip} , as indicated by dashed lines in Fig.5g and 5h.

Along the scan line 1, the changes in the number of charges is the only phenomenon affecting transport, hence they are easy to follow. Along line 2 however, this is less trivial. The tip that depletes the 2DEG underneath is scanned above preferential electron trajectories (branching). As a consequence, Fabry-Pérot interference fringes as a function of tip position are visible. Nevertheless, changes in the number of charges can still be visualized by differentiating the signal with respect to V_g , and interference can be highlighted by differentiating the signal with respect to d_{tip} . By placing dashed lines corresponding to a change in the number of localized charges on Fig.5j and 5k, one can see that a change in this number is correlated with an abrupt phase shift of π in the interference fringes. The most visible case is highlighted in Fig.5l. This case is clearer because the tip is far from the QPC, hence changes in the number of charges are spaced by more than 100 nm in the tip position. When the tip is closer to the QPC, the phase shift is really hard to distinguish because these changes are separated by less than one hundred nanometer, which corresponds to only one or two Fabry-Pérot oscillations. It is therefore very difficult to see a phase shift by π occurring only for one or two interference fringes, which leads to blurred and very large oscillations.

For the sample whose data are discussed in the main text, we were forced to scan the tip close to the QPC due to a dust particle on the sample surface, located at about 1 μm away from the QPC. In this region, the number of localized charges changes rapidly with tip position and produce several phase shifts in the interference pattern. In Fig. 4c of the main paper, there are probably two changes in the number of localized charges that produce the two distortions visible in the interference pattern.

The abrupt phase shift observed in TSGM as a function of gate voltage at the very pinch-off (Fig. 4d of the main paper) looks really similar to those observed in SGM in previous samples, but it differs in two main aspects:

- It evolves parallel to the QPC pinch-off line controlled by the cross-talk between the split gate and the scanning gate, whereas other observed phase shifts follow a different evolution (the green dashed lines in Fig.5 are not parallel the line corresponding to the cross-talk)

- It is visible at very low transmission, lower than for any phase shift observed by the authors in their previous works.

These two differences suggest that, in the regime of very low transmission, the localized charges are not sensitive to the tip potential, whose only effect is to curve the pinch-off line.

A more puzzling property of this phase shift is that it is only visible in the thermovoltage and not in the conductance. We currently have no explanation for this anomalous behavior. Even if we know that the Mott's law does not hold in this regime of strong electron interactions, one would not expect such an all-or-nothing difference (phase shift or no phase shift) between the thermopower and the conductance. This really surprising difference indicates indeed that the thermopower and the conductance are significantly different spectroscopic tools, and may be sensitive to different aspects of an interacting mesoscopic system.

VI. CLASSICAL ELECTROSTATIC SIMULATIONS

We perform self-consistent classical electrostatic simulations to estimate how a localized state could form in our geometry, near pinch-off. The mesh grid is computed using Gmsh (<http://gmsh.info>) and the electrostatic problem is solved self-consistently using a modified version of MaxFEM (<http://www.usc.es/en/proyectos/maxfem>), an electromagnetic simulation software based on the finite element method.

The system is modeled by a 2DEG of density $2.5 \times 10^{11} \text{ cm}^{-2}$, separated by a 100 nm-thick AlGaAs layer from the surface, on top of which 300 nm-wide and 100 nm-thick metallic gates are defined. The local density is computed in the Thomas-Fermi approximation and represented as a colormap in Fig.6a-c for different gate voltages. The surface occupied by each electrons is then represented by a circle whose diameter is equal to $\sqrt{1/n_{2D}}$.

To estimate how many electrons are likely to localize in the QPC channel, we compare these results with the expected criterion for Wigner crystallization. As the density of an electronic system is reduced, the Wigner-Seitz radius r_s , defined as the ratio of half the inter-particle distance to the Bohr radius a_B , enlarges ($a_B = 10 \text{ nm}$ in GaAs). When r_s overcomes the critical value r_{sc} , the electronic system undergoes a phase transition from a Fermi liquid to a Wigner crystal¹². In two dimensions, numerical estimates of r_{sc}^{2D} indicate a value close to 37¹³, which is never reached in our simulations. The Fermi liquid description therefore holds for the 2D regions. In one dimension however, the value of r_{sc}^{1D} depends on the confinement

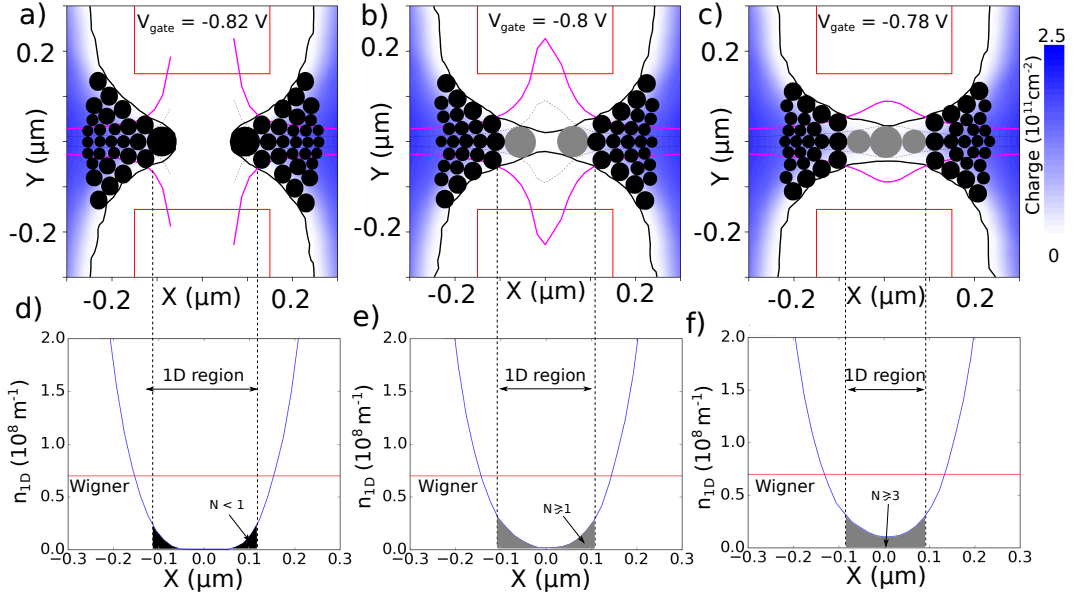


FIG. 6: Self-consistent electrostatic simulations for different gate voltages: (a) $V_{gate} = -0.82$ V. (b) $V_{gate} = -0.8$ V. (c) $V_{gate} = -0.78$ V. The Fermi energy is $E_F = 8$ meV. Red lines: gates geometry. Colorscale: 2D-density in the 2DEG plane. The spacing between the dashed lines indicate the electron spacing, and each black or grey disk contains one electron charge. The spacing between the two pink lines give the Fermi wavelength, and the 1D region corresponds to the region where these lines intersect with the zero-density black lines. The blue lines in (d-f) represent the 1D electron density integrated along the y -direction. In the 1D region (dashed lines), the 1D density is below the critical value for 1D Wigner crystallization.

potential strength but is closer to unity¹⁴. In Ref.⁸, r_{sc}^{1D} has been estimated to ~ 0.7 , and this criterion was shown to be reached below the first conductance plateau, yielding a few crystallized electrons in the channel. In Figs. 6d to 6f, we show estimates of the 1D density n_{1D} in the one-dimensional region, and indicate the region where the electron transport is effectively 1D, i.e. where only one transverse electronic mode is permitted. In this 1D region, the 1D density is below the critical density $1/(2r_{sc}^{1D} a_B)$ where we can expect Wigner crystallization (below the red line). In the following, we calculate how many electrons the crystallization region may contain. This estimation shows that no crystallization is expected for a completely closed QPC (Fig.6a,d), since both 1D regions on the two sides of the QPC

barrier contain less than one electron charge. As the QPC opens, the density in the two 1D regions on both sides of the barrier increase, up to a point where each of these regions may contain one electron charge (Fig.6b,e). For larger opening, the crystallization regions merge across the full QPC length and becomes large enough to contain 3 electrons (Fig.6c,f).

Though a more accurate calculation including quantum effects would be required to estimate the exact behavior of localized electrons^{15,16}, our simple approach indicates that one electron may be localized in each 1D region of the channel near QPC pinch-off (Fig.6b), but this situation is not favored anymore as the QPC closes (Fig.6a). Therefore the energy level corresponding to this spontaneously localized state may evolve in a very peculiar way with the QPC opening, and could correspond to the behavior of the phase shift observed in our TSGM experiment.

-
- ¹ V. C. Karavolas and P. N. Butcher, *Journal of Physics: Condensed Matter* **3**, 2597 (1991).
 - ² R. Fletcher, P. T. Coleridge, and Y. Feng, *Phys. Rev. B* **52**, 2823 (1995).
 - ³ M. Schmidt, G. Schneider, C. Heyn, A. Stemann, and W. Hansen, *Journal of Electronic Materials* **41**, 1286 (2012).
 - ⁴ A. Mittal, R. Wheeler, M. Keller, D. Prober, and R. Sacks, *Surface Science* **361**, 537 (1996).
 - ⁵ P. J. Price, *Journal of Applied Physics* **53**, 6863 (1982).
 - ⁶ S. Jezouin, F. D. Parmentier, A. Anthore, U. Gennser, A. Cavanna, Y. Jin, and F. Pierre, *Science* **342**, 601 (2013).
 - ⁷ E. Sivre, A. Anthore, F. D. Parmentier, A. Cavanna, U. Gennser, A. Ouerghi, Y. Jin, and F. Pierre, *Nat. Phys.* **14**, 145 (2017).
 - ⁸ B. Brun, F. Martins, S. Faniel, B. Hackens, G. Bachelier, A. Cavanna, C. Ulysse, A. Ouerghi, U. Gennser, D. Mailly, S. Huant, V. Bayot, M. Sanquer, and H. Sellier, *Nat. Commun.* **5**, 4290 (2014).
 - ⁹ S. M. Cronenwett, *Coherence, charging and spin effects in quantum dots and quantum point contacts*, Ph.D. thesis, Harvard University (2001).
 - ¹⁰ M. J. Iqbal, *Electron many-body effects in quantum point contacts*, Ph.D. thesis, Groningen University (2014).

- ¹¹ B. Brun, *Electron interactions in mesoscopic physics : Scanning Gate Microscopy and interferometry at a quantum point contact*, Ph.D. thesis, Université de Grenoble (2014).
- ¹² E. Wigner, Phys. Rev. **46**, 1002 (1934).
- ¹³ B. Tanatar and D. M. Ceperley, Phys. Rev. B **39**, 5005 (1989).
- ¹⁴ L. Shulenburger, M. Casula, G. Senatore, and R. M. Martin, Phys. Rev. B **78**, 165303 (2008).
- ¹⁵ A. D. Güçlü, C. J. Umrigar, H. Jiang, and H. U. Baranger, Phys. Rev. B **80**, 201302 (2009).
- ¹⁶ T. Rejec and Y. Meir, Nature **442**, 900 (2006).
-